ZHOU, Y., WANG, S., XIE, Y., SHEN, X. and FERNANDEZ, C. 2023. Remaining useful life prediction and state of health diagnosis for lithium-ion batteries based on improved grey wolf optimization algorithm-deep extreme learning machine algorithm. *Energy* [online], 285, article 128761. Available from: https://doi.org/10.1016/j.energy.2023.128761

Remaining useful life prediction and state of health diagnosis for lithium-ion batteries based on improved grey wolf optimization algorithm-deep extreme learning machine algorithm.

ZHOU, Y., WANG, S., XIE, Y., SHEN, X. and FERNANDEZ, C.

2023

Energy

Remaining useful life prediction and state of health diagnosis for lithium-ion batteries based on Improved Grey Wolf Optimization Algorithm-Deep Extreme Learning Machine Algorithm

--Manuscript Draft--

Manuscript Number:	EGY-D-23-05143R2
Article Type:	Full length article
Keywords:	Lithium-ion batteries; State of health; health indicator; grey wolf algorithm; deep extreme learning machine
Corresponding Author:	Shunli Wang, Prof.Dr. Mianyang, CHINA
First Author:	yifei zhou
Order of Authors:	yifei zhou
	Shunli Wang
	Yanxin Xie
	Xianfeng Shen
	Carlos Fernandez
Abstract:	The prediction of SOH for Lithium-ion battery systems determines the safety of Electric vehicles and stationary energy storage devices powered by LIBs. State of health diagnosis and remaining useful life prediction also rely significantly on excellent algorithms and effective indicators extraction. Since the data obtained from the aging experiment of Lithium-ion batteries is rich in electrochemical and dynamic information, useful health indicators can be extracted for SOH and RUL prediction of machine learning. This paper presents a method for predicting SOH and RUL based on a data-driven model of deep extreme learning machine based on improved Grey Wolf optimization algorithm. Firstly, GWO algorithm is improved by piecewise chaotic distribution and sine-cosine algorithm, and then multi-layer superposition is performed on an extreme learning machine to form DELM. Additionally, the experimental data of the Center for Advanced Life Cycle Engineering data set was extracted and analyzed, the aging state of batteries was analyzed and verified from multiple scales, and the strong correlation of aging characteristics was extracted and verified. After that, the model was driven by the extracted health indicators, and the accuracy and robustness of the results were checked.

Credit Author Statement

Yifei Zhou: Writing - Original Draft, Software, Conceptualization, Methodology. **Shunli Wang:** Supervision. **Yanxing Xie:** Validation. **Xianfeng Shen:** Visualization. **Carlos Fernandez:** Writing - Review & Editing.

Highlights

- The battery charging and discharging data are deeply analyzed to extract multi-level health indicators.
- The DELM data-driven model based on improved GWO algorithm for RUL prediction and SOH diagnosis is proposed.
- The aging state of the battery was analyzed and the correlation between the health indicators and the capacity was verified.
- The accuracy and robustness of the model are verified by the extracted health indicators.

Remaining useful life prediction and state of health diagnosis for Lithium-ion batteries based on Improved Grey Wolf Optimization Algorithm-Deep Extreme Learning Machine Algorithm

Yifei Zhou[a], Shunli Wang[a]*, Yanxing Xie[a], Xianfeng Shen[a], Carlos Fernandez[b]

[a]School of Information Engineering, Engineering and Technology Center, Southwest University of Science and Technology, Mianyang, China; [b]School of Pharmacy and Life Sciences, Robert Gordon University, Aberdeen, UK.

Shunli Wang*, School of Information Engineering, Engineering and Technology Center, Southwest University of Science and Technology. 497420789@qq.com

Abstracts

The prediction of SOH for Lithium-ion battery systems determines the safety of Electric vehicles and stationary energy storage devices powered by LIBs. State of health diagnosis and remaining useful life prediction also rely significantly on excellent algorithms and effective indicators extraction. Since the data obtained from the aging experiment of Lithium-ion batteries is rich in electrochemical and dynamic information, useful health indicators can be extracted for SOH and RUL prediction of machine learning. This paper presents a method for predicting SOH and RUL based on a data-driven model of deep extreme learning machine based on improved Grey Wolf optimization algorithm. Firstly, GWO algorithm is improved by piecewise chaotic distribution and sine-cosine algorithm, and then multi-layer superposition is performed on an extreme learning machine to form DELM. Additionally, the experimental data of the Center for Advanced Life Cycle Engineering data set was extracted and analyzed, the aging state of batteries was analyzed and verified from multiple scales, and the strong correlation of aging characteristics was extracted and verified. After that, the model was driven by the extracted health indicators, and the accuracy and robustness of the results were checked.

Keywords: lithium-ion batteries; state of health; health indicator; grey wolf algorithm; deep extreme learning machine;

1. Introduction

To cope with the double pressure of the environment and energy and the urgent need to accomplish the carbon neutrality target, countries all over the world consider the development and utilization of new energy as an important strategy for sustainable development. This strategy has led to the increasing popularity of new energy vehicles. And Lithium-ion batteries (LIBs) as the heart of new energy vehicles at the same time also attracted more attention. In more recent years with the gradual progress of battery technology, the battery as the main power supply or energy storage component of the device has been widely used [1]. Lithium-ion batteries are widely used because of their high energy density, small package size and weight, no memory, low self-discharge rate, and high adaptability. Therefore the monitoring of real-time battery state of health (SOX) and remaining useful life (RUL) in the battery management system (BMS) has been the key concern [2]. Different charge-discharge distributions, ambient temperature, positive and negative electrode materials, capacity regeneration, and other factors lead to different battery capacity aging trends, the aging mechanism is shown in Figure 1 [3]. The complexity and nonlinearity of battery capacity aging are challenging to predict RUL accurately [4, 5]. The diversity and uncertainty of external operating conditions and internal side reactions of the LIBs make an accurate estimation of State of Health (SOH) a challenge [6]. Various methods for online capacity estimation are investigated. These methods mainly use external characteristic parameters for SOH and RUL prediction and include empirical-based methods, model-based methods, data-driven methods, and characteristic signal analysis methods.

To describe the aging behavior of the battery, a physical or empirical model of the battery is created mathematically. The model created using this method typically consists of a sequence of algebraic and differential equations. The SOH and RUL prediction model designed for a specific system only distinguishes the empirical-based method [7]. This paper [8] proposes a new hybrid Elman-Long Short-Term Memory (LSTM) method for forecasting the remaining battery life by combining the empirical model decomposition algorithm, long and short-term memory, and Elman neural network. In this paper [9], a fusion technique consisting of a correlation vector machine and particle filter is proposed and used to construct a battery aging model for RUL prediction. In this paper [10], several candidate health indicators are extracted from the peaks and valleys of part of the incremental capacity curve and screened. The fine-tuning process of particle swarm optimization based deep belief network is described in detail, and compared with three classical deep networks in terms of error and time consumption. In addition, this paper [11] introduces battery State of charge (SOC) as a factor to be included in the calendar life prediction model combined with an impedance-based electrothermal model. Nevertheless, operational conditions in real-world applications are frequently complicated and convergent, so empirically based approaches alone cannot reliably detect battery degeneration.

The aging mechanism of Lithium-ion batteries is diverse and complex, and it is closely related to many interacting factors such as battery type, electrochemical reaction stage, and operating conditions. This literature [12] systematically summarizes the mechanism of action and diagnosis of Lithium battery aging. The model-based approach, on the other hand, consists mainly of an equivalent circuit model (ECM) and an electrochemical model. ECM is more suitable for SOC estimation and the electrochemical model is more suitable for degradation analysis and SOH estimation [13, 14]. This paper [15], presents a reduced-order electrochemical model of an observer for estimating cathode and anode potentials, which requires only terminal voltages to track the cathode and anode po potentials and their internal charge concentrations. This work [16] investigates the main stress factors affecting the polarization process of the cell based on the conventional single-particle model. The main stress factors are used to compensate for and correct the key parameters of polarization to establish a more accurate single-particle model. However, building an accurate model of the cell mechanism is time-consuming and computationally expensive.

Data-driven modeling is the direct use of historical data to build predictive models without relying on specific physical models through statistical and machine learning theories [17, 18]. Therefore, the approach based on data-driven models is more easily applied to different situations. This literature [19] proposes an improved ISSA-LSTM-based data-driven model and demonstrates experimentally that its RUL prediction method is more accurate and robust, which contributes to the rational use of Lithium-ion batteries. This study [20] proposes a novel hybrid model based on adaptive feature separable convolution (AFSC) and convolutional long and short-term memory (ConvLSTM) networks to improve the accuracy of RUL prediction and the interpretability of the model. This paper [21] introduces a Gaussian process regression for multi-step prediction based on the codec model, improves the codec fusion method, and smoothes the training set using the Savitzky-Golay method. A new kernel function is designed to further improve computational accuracy. The estimated values of the GNN model are used as PF observations in this paper [22] to generate a grey model of the GNN fusion sliding window based on PF framework (GNN-SGMPF).

Based on the model, the extraction of battery health indicators (HIs) is also an important part of battery health state estimation. This study [23] proposes a new method for HIs extraction based on the *u*-chord curvature model based on a complete analysis of battery aging data. Compared with previous feature extraction methods, this method divides the discharge process into different stages according to the curvature of the discharge curve and extracts many HIs highly relevant to the battery at the discharge plateau stage of the discharge curve. This literature [24] presents a probabilistic approach to battery degradation modeling and health prediction based on features extracted from the charging process using dynamic Bayesian networks (DBN). A voltage-temperature health feature extraction method is proposed [25] to improve the Prognostic and Health Management (PHM) of Lithium-ion batteries by extracting voltage-dependent HIs from partial voltage profiles through the principle that the voltage changes during battery degradation, and it is not necessary to discharge the battery completely. Meanwhile, the battery surface temperature is selected as a thermally dependent health feature because battery aging is influenced by temperature. This paper [26] has three multiscale blocks (MS-BLOCKs) by using a multiscale deep convolutional neural network (MS-DCNN) where three different sizes of convolutional operations are placed on each block in parallel. This structure improves the network's ability to learn complex features by extracting features at different scales.

Based on the above problems and the popularity of data-driven models based on deep learning methods in recent years, this paper proposes a deep limit learning machine algorithm based on an improved grey wolf optimization algorithm and a new feature extraction method with an emphasis on experimental data in battery health feature extraction. And the validity of the model and the strong correlation of the features are verified by bringing in data testing. The novelty and contributions of this study are summarized as follows:

In this paper, it is presented a method based on multi-scale aging feature extraction, as shown in Figure 2, based on an optimized data-driven model constructed using the extracted multiple HIs and combined with the use of the sine-cosine optimization algorithm enhanced with the Grey Wolf optimization algorithm, which proposes a data-driven model for SOH and RUL prediction, optimized for the Deep Extreme Learning Machine. In this work, the accuracy and robustness of the model as well as the reliability of the feature extraction were tested using aging data from 10 battery packs based on two types of batteries at the University of Maryland Center for Advanced Life Cycle Engineering.

The main contributions can be summarized as follows: (1) Using the current curve, voltage curve, and IC curve extracted from the experimental data of ten battery packs, the patterns of curve changes are found to extract the multi-scale battery HIs, and their strong correlation with battery capacity is verified by Pearson's correlation formula; (2) A novel Lithium-ion battery SOH and RUL prediction framework combining sine-cosine and traditional Grey Wolf Optimization (GWO) algorithm is proposed to optimize the deep limit learning machine; (3) Using the optimized deep limit learning machine model, the extracted constant current charging time (CCCT), constant voltage charging time (CVCT), ICCP (IC curve peak) and other relevant aging characteristics and the actual battery capacity are input to build the model, and the prediction results are obtained after training; (4) SOH and RUL analyses are performed on the capacity data predicted by the output of the new driver model to verify the accuracy and robustness of the model by comparing the metrics.

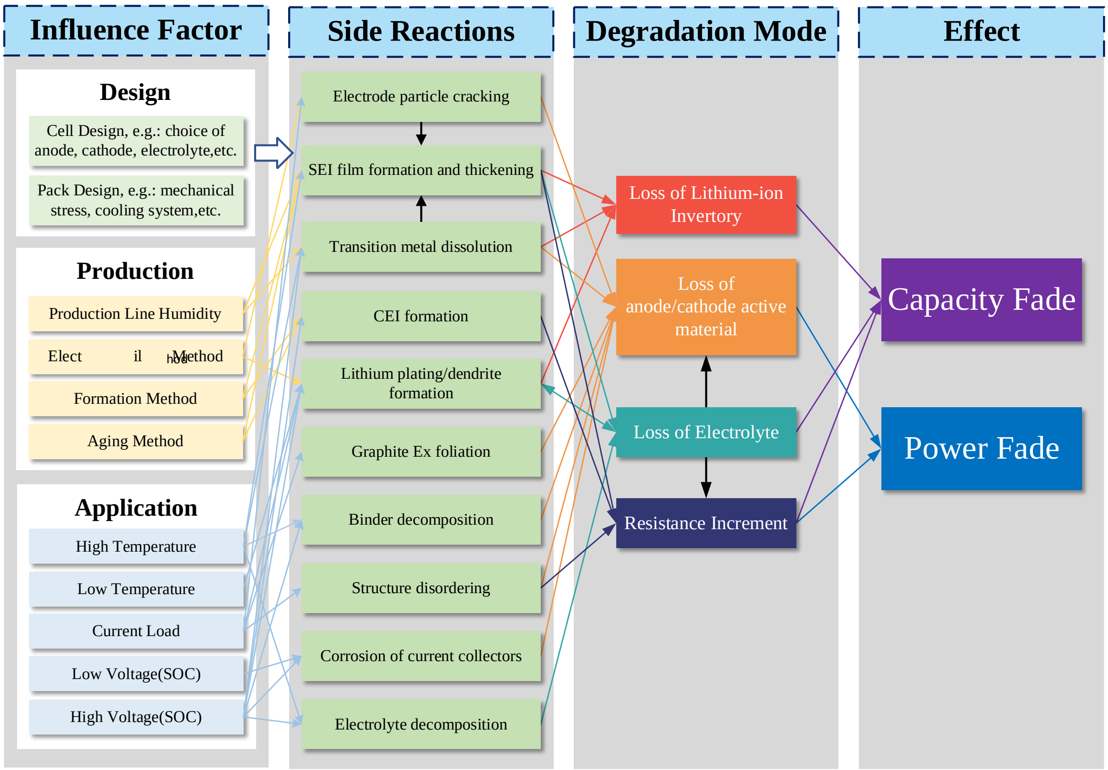

Figure 1. Schematic diagram of Lithium-ion battery aging causative factors and results

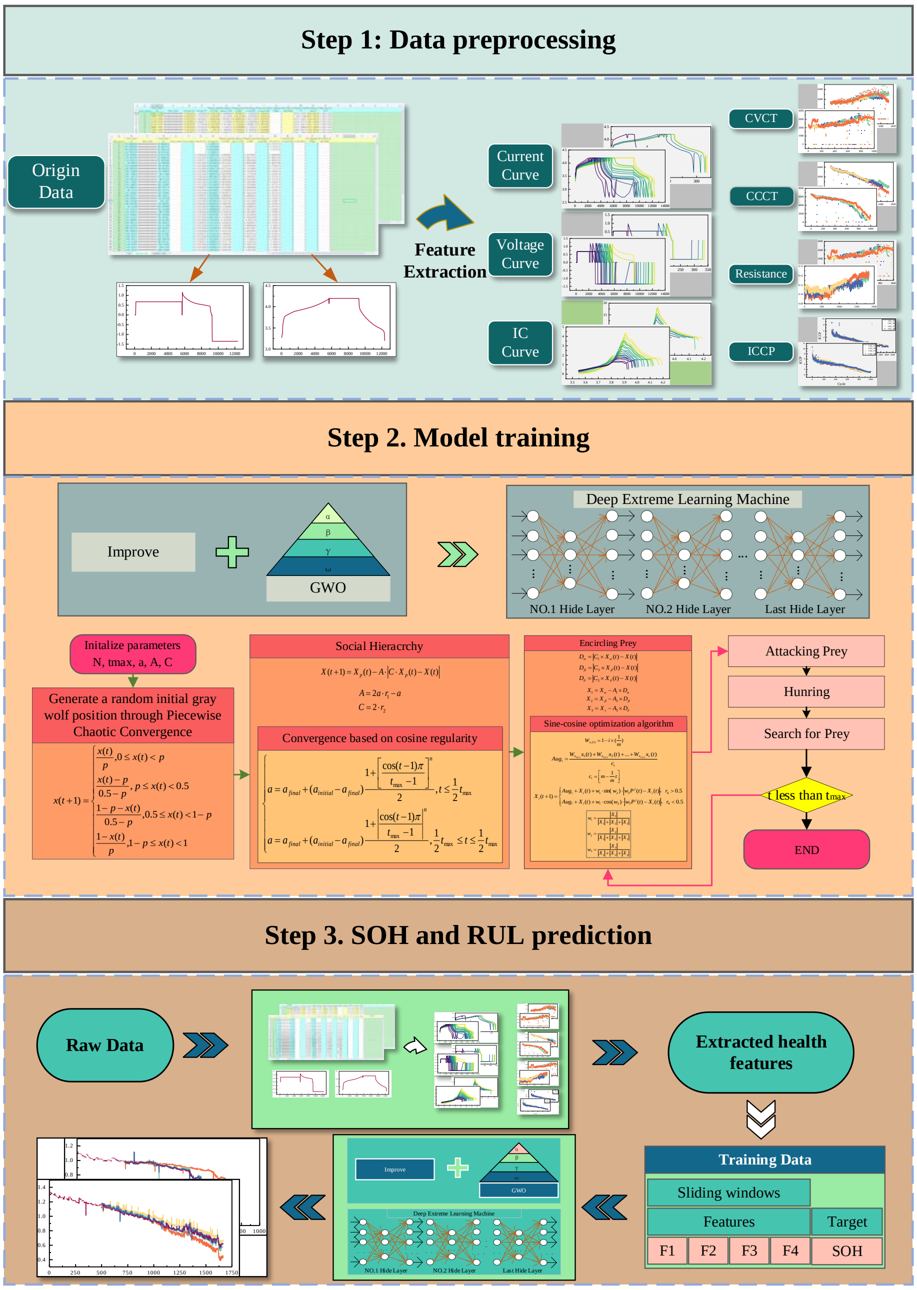

Figure 2. Schematic diagram of the IGWO-DELM algorithm for SOH and RUL prediction

2. Improved GWO-DELM Algorithm

2.1. DELM method

Extreme learning machine (ELM) is a kind of feed-forward neural network, which was first proposed by Prof. Huang Guangbin from Singapore, and the paper pointed out that ELM has good generalization performance and extremely fast learning ability [27]. Unlike traditional neural networks, ELM does not need to adjust the weights based on the directional propagation of the gradient but sets the weights by Moore-Penrose generalized inverse (GIR). The traditional neural network requires the input value multiplied by the weight value plus the bias value for the activation function calculation, and repeats the first three steps at each layer, while ELM does not repeat the calculation, and calculates the output value directly, which makes the operation volume significantly reduced, and replaces the error backpropagation step with one matrix inverse operation is determined once by solving the system of equations. Therefore, instead of using the tried and tested gradient-based algorithm in traditional neural networks, ELM uses randomized input layer weights and biases, and the output layer weights are calculated by generalized inverse matrix theory. The computational procedure of ELM is very similar to that of a standard back-propagation neural network, but the weight matrix between the hidden layer and the output is a pseudo-inverse matrix. The calculation formula is as follows:

$$f_L(x) = \sum_{i=1}^{L} \beta_i \cdot g_i(x) = \sum_{i=1}^{L} \beta_i \cdot g(\omega_i * x_j + b_i),\ j = 1, \ldots, N \tag{1}$$

where L is the number of hidden units, N is the number of training samples, β is the weight vector between the i-th hidden layer and the output, ω is the weight vector between the input and the output, g is the activation Equation (1) expressed in terms of the logistic sigmoid function, b is the bias vector, and x is the input vector.

$$g(x) = \frac{1}{1+e^{-x}} \tag{2}$$

The structure of a typical single implicit layer feedforward neural network is shown in Figure 3, which consists of an input layer, an implicit layer, and an output layer, with full connectivity between the input layer and the implicit layer, and between the implicit layer and the output layer neurons. Among them, the input layer has n neurons, corresponding to n input variables, and the hidden layer has l neurons; the output layer has m neurons, corresponding to m output variables. Let the connection weights w between the input layer and the implicit layer be shown in Equation (3):

$$w = \begin{bmatrix} w_{11} & w_{12} & \cdots & w_{1n} \\ w_{21} & w_{22} & \cdots & w_{2n} \\ \cdots & \cdots & \cdots & \cdots \\ w_{s1} & w_{s2} & \cdots & w_{sn} \end{bmatrix} \tag{3}$$

where w_n denotes the connection weight between the i-th neuron in the input layer and the j-th neuron in the hidden layer.

As shown in Equation (4), the connection weight between the implicit layer and the output layer is

β.

$$\beta = \begin{bmatrix} \beta_{11} & \beta_{12} & \cdots & \beta_{1k} \\ \beta_{21} & \beta_{22} & \cdots & \beta_{2k} \\ \cdots & \cdots & \cdots & \cdots \\ \beta_{j1} & \beta_{j2} & \cdots & \beta_{jk} \end{bmatrix} \tag{4}$$

where self β_{jk} denotes the connection weight between the j-th neuron of the hidden layer and the k-th neuron of the output layer.

As shown in Equation (5), the threshold b of the hidden layer neuron is:

$$b = \begin{bmatrix} b_1 \\ b_2 \\ \cdots \\ b_s \end{bmatrix} \tag{5}$$

As shown in Equation (6), let the input matrix X and output matrix Y of the training set with Q samples be:

$$X = \begin{bmatrix} x_{11} & x_{12} & \cdots & x_{1Q} \\ x_{21} & x_{22} & \cdots & x_{2Q} \\ \cdots & \cdots & \cdots & \cdots \\ x_{n1} & x_{n2} & \cdots & x_{nQ} \end{bmatrix}$$

$$Y = \begin{bmatrix} y_{11} & y_{12} & \cdots & y_{1Q} \\ y_{21} & y_{22} & \cdots & y_{2Q} \\ \cdots & \cdots & \cdots & \cdots \\ y_{m1} & y_{m2} & \cdots & y_{mQ} \end{bmatrix} \tag{6}$$

From Figure 3, let the activation function of the hidden layer neuron be $g(x)$, then the output T of the network is shown in Equation (7):

$$T = [t_1, \ldots, t_Q]_{m*Q}$$

$$t_j = [t_{1j}, \ldots, t_{mj}]^T = \begin{bmatrix} \sum_{i=1}^{t} \beta_{i1} g(w_i x_i + b_i) \\ \sum_{i=1}^{t} \beta_{i2} g(w_i x_i + b_i) \\ \cdots \\ \sum_{i=1}^{t} \beta_{im} g(w_i x_i + b_i) \end{bmatrix}, j = 1, 2, \ldots, Q \tag{7}$$

The above formula can be expressed as $H^{\beta}=T^{T}$.

Where T^T is the transpose of the matrix T, H is the output matrix of the hidden layer of the neural network. The specific form is shown in Equation (8) below:

$$H(w_1,...w_i,b_1,...,b_l,x_1,...,x_Q) = \begin{bmatrix} g(w_1*x_1+b_1) & g(w_1*x_1+b_2) & ... & g(w_1*x_1+b_l) \\ g(w_1*x_2+b_1) & g(w_1*x_2+b_2) & ... & g(w_1*x_2+b_l) \\ ... & ... & ... & ... \\ g(w_1*x_Q+b_1) & g(w_1*x_Q+b_2) & ... & g(w_1*x_Q+b_l) \end{bmatrix} \tag{8}$$

Autoencoder (AE) can copy the input to the output after training. Training an autoencoder is unsupervised because no labeled data is required. Therefore, the idea of AE is applied to ELM so that the input data of ELM is also used for the output, i.e., the output $Y = X$. The network structure of the Extreme Learning Machine ELM-AE, which is used as an autoencoder, is shown in Figure 3.

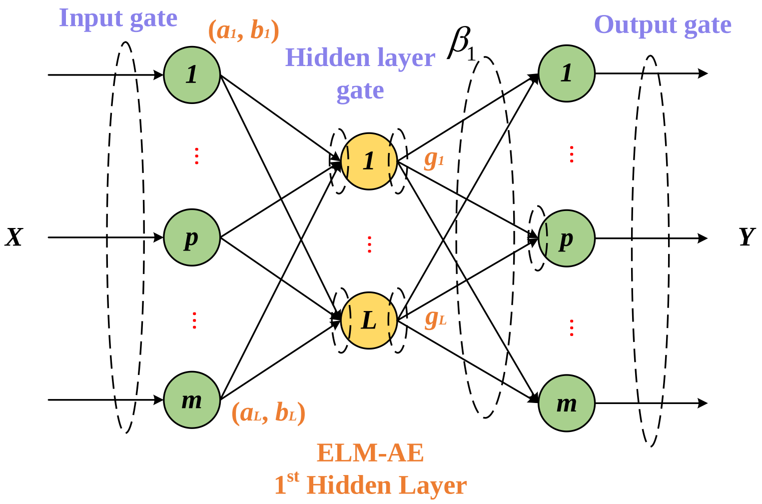

Figure 3. Extreme Learning Machine Auto-Encoder Schematic

When m is greater than L in Figure 3, ELM-AE realizes dimensional compression and maps the high-dimensional data into low-dimensional feature expressions; when m is equal to L, ELM-AE obtains equal-dimensional feature expressions. When m is smaller than L, ELM-AE successfully expresses the high-dimensional features of the original data in a sparse way. In summary, ELM-AE is a generalized approximator characterized by making the output of the network the same as the input and randomly generating orthogonal input parameters (a_i, b_i) for the hidden layer. Orthogonalization has the following advantages, according to the *J-L* (Johnson-Lindensrauss) theorem, orthogonalization of weights and biases can map the input data to spaces of different or equal dimensions, thus enabling the feature representation of different functions. The orthogonal design of weights and biases removes noise beyond the features and makes the features more homogeneous and linearly independent, thus enhancing the generalization ability of the system.

The output of ELM-AE can be expressed in the following expression:

$$x_j = \sum_{i=1}^{L} \beta_i g(a_i, b_i, x_j), a_i \in R^m, \beta_i \in R^m, j = 1,2,\dots,N, a^T a = I, b^T b = 1 \tag{9}$$

Where a is the matrix of a_i and b is b_i. The output weight of the hidden layer is:

$$\beta = (\frac{I}{C} + H^T H)^{-1} HTX \tag{10}$$

Where $X = [x_1, \dots, x_N]$ is the input data.

In this paper, the DELM is built based on ELM combined with the deep learning method. Under the condition of inheriting the high efficiency of deep learning, the reverse cycle optimization of traditional deep learning is replaced by ELM-AE, which further improves the efficiency of the algorithm, encapsulates multiple ELM-AE, improves the precision and accuracy, and makes it easier to solve complex problems in real-time.

According to the characteristic capability of ELM-AE, it is taken as the basic unit of the deep extreme learning machine DELM [28]. The same as the traditional deep learning algorithm, DELM also uses the hierarchical greedy training method to train the network. The input weights of each hidden layer in DELM are initialized with ELM-AE and hierarchical unsupervised training is performed. DELM doesn't require the reverse fine-tuning procedure, in contrast to the conventional deep learning method.

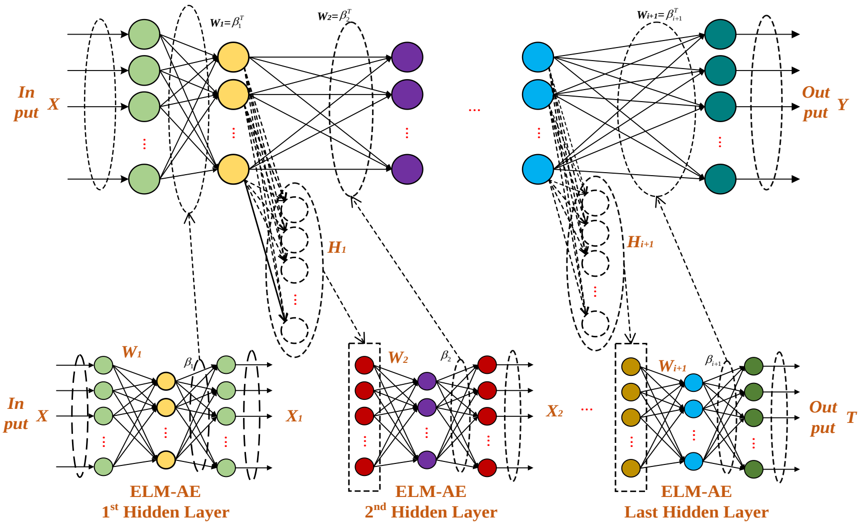

Figure 4. Deep learning combined with extreme learning machine works schematically

The idea of DELM is to minimize the reconstruction error so that the output can be infinitely close to the original input. Through the training of each layer, the advanced features of the original data can be learned. Figure 4 describes the training process of the DELM model. The input data sample X is taken as the target output ($X_1 = X$) of the first ELM-AE, and then the output weight β_1 is calculated.

Then, the output matrix H_1 of the first hidden layer of DELM is taken as the input and target output ($X_2 = X$) of the next ELM-AE, and the training is conducted layer by layer by layer and the last layer is trained with ELM. Equation (4) is used to solve the output weight β_{i+1} of the last hidden layer of DELM. In Figure 4, H_{i+1} is the output matrix of the last hidden layer, T is the sample label, and the input weight matrix of each hidden layer of H_{i+1} is $W_{i+1} = \beta_{i+1}^T$.

The idea of DELM is to minimize the reconstruction error so that the output can be infinitely close to the original input. Through the training of each layer, the advanced features of the original data can be learned.

2.2. SCA-GWO Algorithm

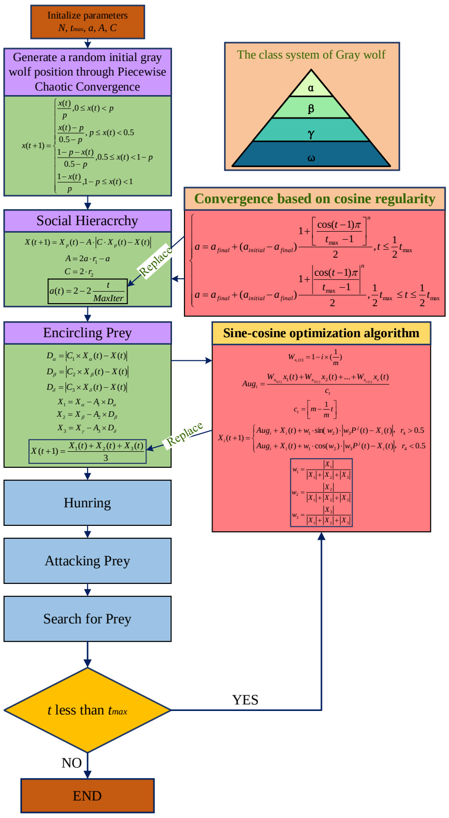

Figure 5. Schematic diagram of the improved GWO algorithm

2.2.1. Piecewise Chaos Mapping

The more uniform the distribution of the initial population in the search space, the better it is for improving the optimization efficiency and solution accuracy of the algorithm [29]. Chaos theory has been widely introduced into swarm intelligence algorithms to enhance the diversity of the initial population to improve the optimization performance of the algorithm because of its randomness, ergodicity, and non-repetition. Compared with random search, chaos theory can perform a comprehensive search of the search space. In summary, to make the initial population individuals utilize the information of the solution space as much as possible, this paper introduces the Piecewise (PW) Chaos mapping in chaos theory to improve the population initialization of GWO algorithm, whose mathematical model is shown in Equation (11).

$$X(t+1)=\begin{cases}\dfrac{X(t)}{p}, 0\le X(t)<p\\ \dfrac{X(t)-p}{0.5-p}, p\le X(t)<0.5\\ \dfrac{1-p-X(t)}{0.5-p}, 0.5\le X(t)<1-p\\ \dfrac{1-X(t)}{p}, 1-p\le X(t)<1\end{cases} \tag{11}$$

where p is taken to be 0.4 and $X(t)$ is a random number from 0 to 1.

2.2.2. GWO Algorithm

Grey Wolf Optimization Algorithm (GWO), inspired by the Grey Wolf. GWO algorithm simulated the leadership hierarchy and hunting mechanism of natural grey wolves [30]. Four types of grey wolves, such as α, β, λ and ω, were used to simulate the leadership class. In addition, the three main steps of hunting were realized: Finding prey, Surrounding prey, and Attacking prey.

In the algorithm, Wolf α is regarded as the optimal solution, Wolf β and Wolf λ as the second and third best solutions, and the remaining candidate solutions are assumed to be ω. In the GWO algorithm, Wolf α, β and λ lead the hunting and Wolf ω follows them.

Encircling prey

During hunting, the behavior of grey wolves that round up prey is defined as follows.

$$X(t+1)=X_p(t)-A\cdot\left|C\cdot X_p(t)-X(t)\right| \tag{12}$$

X and X_p are the position vectors of the individual gray wolf and the prey, respectively, t is the current iteration number, and A and C are the coefficient vectors as expressed in Equation (14).

$$\begin{gathered}A=2a\cdot r_1-a\\ C=2\cdot r_2\end{gathered} \tag{13}$$

r_1 and r_2 are random vectors between [0,1] respectively. a is called the distance control parameter and its value decreases linearly from 2 to 0 as the number of iterations increases, as expressed in

Equation (14).

$$a(t) = 2 - 2\frac{t}{MaxIter} \tag{14}$$

MaxIter indicates the maximum number of iterations.

$$\begin{aligned} D_\alpha &= \left|C_1 \times X_\alpha(t) - X(t)\right| \\ D_\beta &= \left|C_2 \times X_\beta(t) - X(t)\right| \\ D_\delta &= \left|C_3 \times X_\delta(t) - X(t)\right| \end{aligned} \tag{15}$$

Where D_α, D_β, and D_δ are the distances between Wolf α, β, δ, and other individuals.

Attacking prey

The mathematical model of a wolf pack attacking its prey is shown in the following equation.

$$\begin{aligned} X_1 &= X_\alpha - A_1 \times D_\alpha \\ X_2 &= X_\beta - A_2 \times D_\beta \\ X_3 &= X_\delta - A_3 \times D_\delta \end{aligned} \tag{16}$$

$$X(t+1) = \frac{X_1(t) + X_2(t) + X_3(t)}{3} \tag{17}$$

$$\begin{aligned} w_1 &= \frac{|X_1|}{|X_1| + |X_2| + |X_3|} \\ w_2 &= \frac{|X_2|}{|X_1| + |X_2| + |X_3|} \\ w_3 &= \frac{|X_3|}{|X_1| + |X_2| + |X_3|} \end{aligned} \tag{18}$$

Where w_1, w_2, and w_3 are the weights occupied by wolves α, β, δ. X_α, X_β, and X_δ are the position vectors of α, β and δ. The calculations of A_1, A_2, and A_3 are similar to those of A, C_1, C_2, and C_3 are similar to those of C.

Study found that when $|A| > 1$, the grey Wolf group will expand the search scope to find prey, namely global searching and fast convergence rate; When the $|A| < 1$, the grey Wolf population will shrink the search scope to attack their prey, the local search, slow convergence speed. Therefore, the size of A is closely related to the global and local search capabilities of GWO algorithm. It can be seen from Equation (13) that A changes with the change of convergence factor a, which linearly decreases from 2 to 0 with the number of iterations. However, the algorithm is not linear in the process of continuous convergence, so it can be seen that the linear decreasing convergence factor cannot fully reflect the actual optimization search process. Therefore, this paper proposes a convergence factor based on the cosine law of change, whose modified expression is shown in Equation (19):

$$\begin{cases} a = a_{final} + (a_{initial} - a_{final}) \dfrac{1 + \left[\dfrac{\cos(t-1)\pi}{t_{\max} - 1} \right]^n}{2}, t \le \dfrac{1}{2} t_{\max} \\ a = a_{final} + (a_{initial} - a_{final}) \dfrac{1 + \left| \dfrac{\cos(t-1)\pi}{t_{\max} - 1} \right|^n}{2}, \dfrac{1}{2} t_{\max} \le t \le t_{\max} \end{cases} \tag{19}$$

Where $a_{initial}$ and a_{final} are the initial and final values of the convergence factor a. In this paper, $a_{initial} = 2$, $a_{final} = 0$, t is the number of iterations, t_{max} is the maximum number of iterations, n is the declining index, and $0 < n \le 1$. The transformation of a is shown in Figure 5.

As can be seen from Figure 6, the image of the original convergence factor a decreases linearly and decreases at the same rate in the iteration process, while the image of the improved convergence factor a is a curve based on the law of cosine change, which decreases slowly in the early iteration, making the convergence factor a maintain a large value for a long time, to improve the search efficiency. In the later iteration period, the decrease is faster, so that A can keep A small value for a long time so that a can keep a small value for long time, to improve the search accuracy. Therefore, the global search ability and local search ability of the algorithm are balanced. Therefore, Equation (19) is used instead of Equation (14) to improve the ability of the algorithm to find the global optimal.

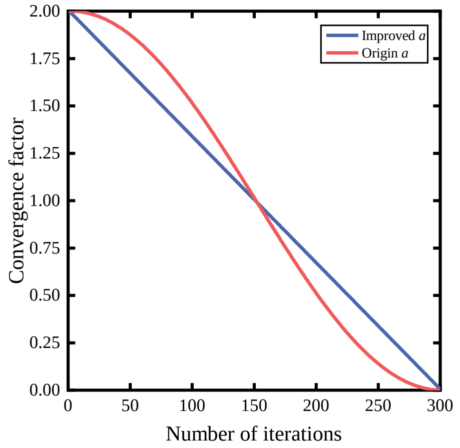

Figure 6. Comparison chart of optimization parameters a

2.2.3. Sine-cosine optimization algorithm

The iteration strategy is summarized into two threads: global search and local development. In the global search thread, a large random wave is applied to the solution in the current solution set to search the unknown region in the solution space [31]. In the local development thread, a weak random perturbation is applied to the solution set to adequately search the neighborhood of the current solution.

SCA uses the periodic volatility of sine and cosine functions to construct an iterative equation to realize the global search and local development of two thread functions. Through this concise update iteration equation, perturbation is applied and the solution set is updated. The specific iteration equation is divided into the following.

Sine iterative or cosine iterative equations of two kinds:

$$\begin{aligned} X_i(t+1) &= X_i(t) + r_1 \cdot \sin(r_2) \cdot \left| r_3 P^j(t) - X_i(t) \right| \\ X_i(t+1) &= X_i(t) + r_1 \cdot \cos(r_2) \cdot \left| r_3 P^j(t) - X_i(t) \right| \end{aligned} \tag{20}$$

Where t represents the number of current iterations, $X_j^i(t)$ represents the component of the position of individual i in the t-th iteration in the j-th dimension, r_1, r_2, and r_3 are random parameters, r_1 is determined by the update function, $r_2 \sim U\,[0, 2\pi]$ and $r_3 \in (0, \infty)$, $P^j(t)$ represents the component of the optimal candidate solution in the j-th dimension in the t-th iteration.

To eliminate the correlation between iteration step size and direction, random parameters $r_4 \sim U\,[0,1]$ were used to combine the above two iteration equations into a complete iteration equation

$$X_i(t+1) = \begin{cases} X_i(t) + r_1 \cdot \sin(r_2) \cdot \left| r_3 P^j(t) - X_i(t) \right|, & r_4 > 0.5 \\ X_i(t) + r_1 \cdot \cos(r_2) \cdot \left| r_3 P^j(t) - X_i(t) \right|, & r_4 < 0.5 \end{cases} \tag{21}$$

To improve the late search oscillation caused by the inertia weight of parent individual information in the iterative process, this paper proposes *a* weight updating mechanism using individual fitness adjustment.

In addition to the current optimal solution and disturbance amplitude, each candidate solution is also affected by *a* weight-adjusted linearly according to its fitness, which depends on the ranking value of its fitness in the candidate set. Candidate sets with higher fitness are assigned higher weights, which have a greater impact on the following generation of candidate solution sets in the updating process:

$$W_{x_i(t)} = 1 - i \times \left(\frac{1}{m_\omega}\right) \tag{22}$$

After determining the weight of each candidate solution, select a part of candidate sets with high fitness to calculate the component of the average bit:

$$Aug_i = \frac{W_{x_{1(t)}} X_1(t) + W_{x_{2(t)}} X_2(t) + \ldots + W_{x_{c(t)}} X_c(t)}{c_t} \tag{23}$$

Where t represents the number of current iterations; $X_i(t)$ represents the candidate solution with the *i*-th fitness in the *t*-th iteration; $W_{x_i(t)}$ represents the weight obtained in the *t*-th iteration; m_ω denotes the size of the candidate solution set (wolf ω).

c_t is the scale of the optimal candidate solution involved in the average position calculation, which decreases with the increase of the number of iterations, the computational equation is shown in Equation (24).

$$c_t = \left\lceil m_\omega - \frac{1}{m_\omega} t \right\rceil \tag{24}$$

To enable the SCA optimization algorithm to be used to optimize the local search and global search capabilities of the grey wolf algorithm, the relevant parameters of Equation (25) of the SCA algorithm are replaced with the relevant parameters in the grey wolf algorithm, allowing the advantages of the SCA algorithm to be utilized.

$$X_i(t+1) = \begin{cases} Aug_i + X_i(t) + w_1 \cdot \sin(w_2) \cdot \left| w_3 P^j(t) - X_i(t) \right|, & r > 0.5 \\ Aug_i + X_i(t) + w_1 \cdot \cos(w_2) \cdot \left| w_3 P^j(t) - X_i(t) \right|, & r < 0.5 \end{cases} \tag{25}$$

Replacing the original random parameters r_1, r_2, and r_3 of SCA with purposeful w_1, w_2 and w_3 of Grey Wolf optimization algorithm makes the algorithm more purposeful in finding the best, and improves the efficiency of the algorithm. w_1, w_2, and w_3 are obtained from Equation (18). r is a random number from 0 to 1 that switches the sine and cosine functions equally. The iterative equation of Equation (17) is replaced by Equation (25) to improve the ability of the algorithm to find the global optimal.

3. Feature Extraction

To accurately predict the state of health of Lithium-ion batteries and better ensure the safety and reliability of Lithium-ion battery use, battery health feature extraction is a very important part. By observing the changing pattern of relevant parameters during the aging process of the battery, the indicators comparable to the changing trend of the capacitance curve are identified and put into the IGWO algorithm for capacity estimation. The accuracy of health feature extraction directly determines the accuracy of capacity prediction.

In this thesis, it was chosen to use the publicly available dataset from the University of Maryland CALCE laboratory and selected data from two batteries, CS2 and CX2, as experimental samples, with the specific parameters of the two batteries as seen in Table 1 [32].

Table 1. Parameters related to battery packs used in battery aging experiments

	Battery name	
	CS2 Battery	CX2 Battery
Battery Parameters	Specifications (Value)	Specifications (Value)
Capacity Rating	1100 mAh	1350 mAh
Cell Chemistry	$LiCoO_2$ cathode (EDS showed trace elements of Manganese)	$LiCoO_2$ cathode (EDS showed trace elements of Manganese)
Weight (w/o safety circuit)	21.1g	28g
Dimensions	5.4 × 33.6 × 50.6 mm	6.6 × 33.8 × 50 mm

All CS2 cells were subjected to the same charging configuration, using a standard constant-current/constant-voltage scheme with a constant-current rate of 0.5°C until the voltage reached 4.2 V, and then held at 4.2 V until the charging current dropped to less than 0.05 A. All cells were charged at a constant-current rate of 0.5°C until the voltage reached 4.2 V and then held at 4.2 V until the charging current dropped to less than 0.05 A. Unless otherwise noted, the discharge cutoff voltage for these cells was 2.7 V. All CS2 cells were randomly numbered and named accordingly. The CS2 cell numbered n is named "CS2_n".CS2_35, CS2_36, CS2_37, and CS2_38 were cycled at a constant current of 1°C, and CS2_33 and CS2_34 were cycled at a constant current of 0.5°C. CX2 was tested in the same way as CS2, respectively, at a constant current of CX2-34, CX2-36, CX2-37, and CX2-38 were cycled at constant flow at 0.5°C. CS2 cells were cycled at constant flow at 0.5°C. Cycle CS2 cells at 0.5°C under constant flow. Cycle CS2 cells at 0.5°C under constant flow. Cycle CS2 cells at 0.5°C under constant flow.

To extract the appropriate HIs, the complete current-voltage curve of a particular cycle of the battery is first analyzed, as seen in the figure below, a complete cycle of current-voltage is roughly divided into three phases, constant current charging section (CCCS), constant voltage charging section (CVCS), and constant current discharging section (CVDS). The current-voltage variation curve in the charge-discharge cycle is shown in Figure 7, and the charge-discharge capacity is shown in Figure 8.

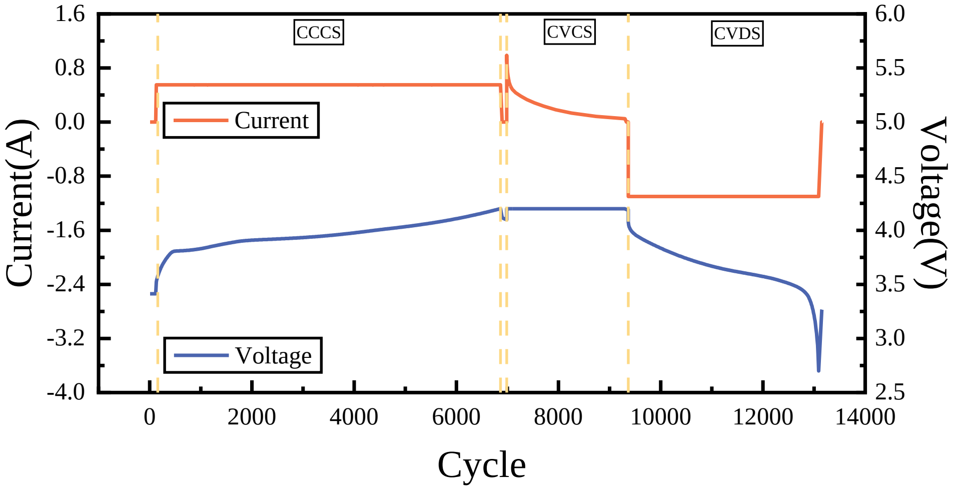

Figure 7. Battery current and voltage curves during the complete charge and discharge cycle

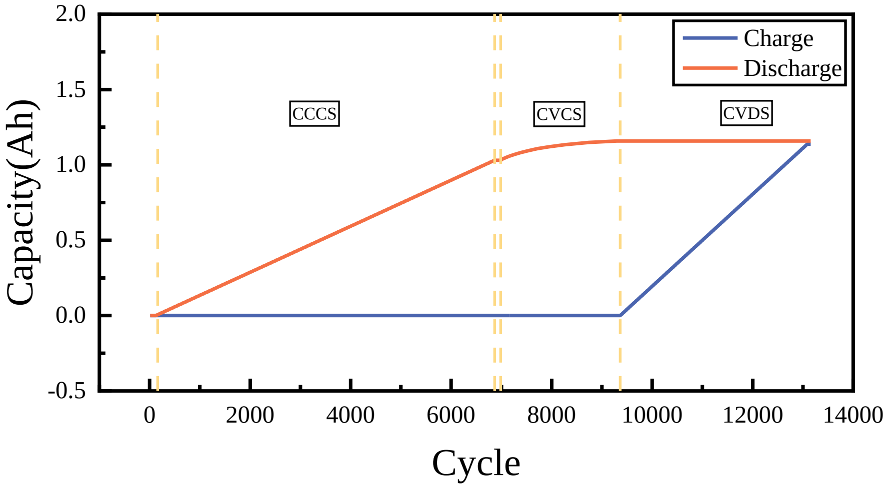

Figure 8. Capacity change curve in the charge and discharge cycle

As seen in Figure 9 and Figure 10, by extracting and analyzing the changes of the current-voltage curves at different cycles, it can be observed that the time to complete a cycle is gradually becoming shorter and the duration of CCCS and CVCS is also significantly shortened as the number of cycles continues to increase as the battery aging experiment proceeds. Therefore, it can be proved that there is a correlation between the aging characteristics and the duration of the charging and discharging process as the battery ages. In this paper, it was chosen to further extract CCCT and CVCT for Pearson correlation analysis.

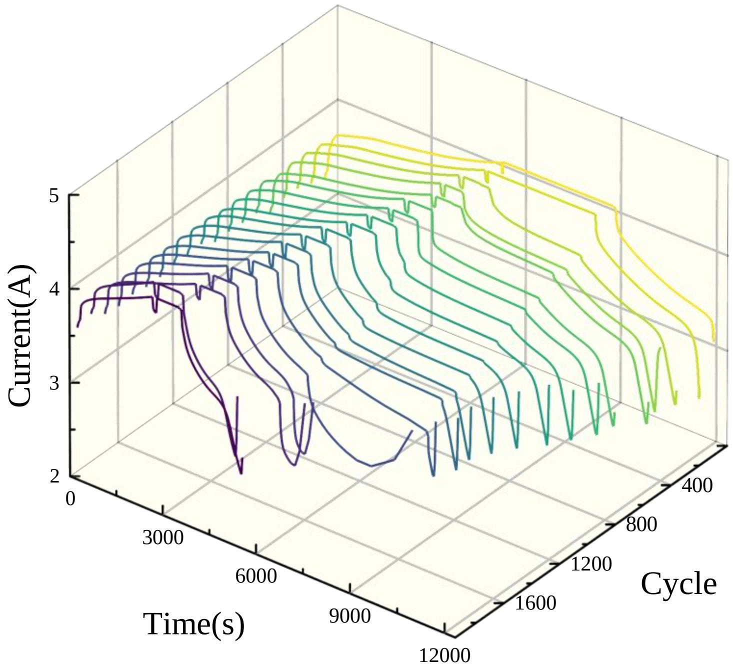

Figure 9. The contrast of voltage curves of different cycles

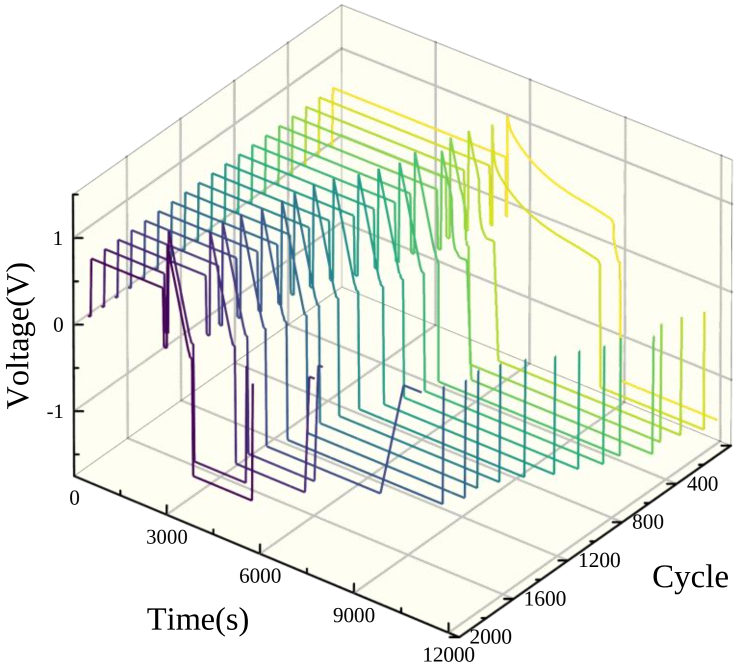

Figure 10. The contrast of current curves of different cycles

From Figure 11 and Figure 12, it can be seen that the CCCT of the extracted cycles showed a decreasing trend and the CVCT showed an increasing trend, with a few protrusions but the overall trend remained consistent. The correlation analysis was performed by Pearson's formula, and the correlation coefficients were all higher than 0.8 indicating that they have high correlation and can be used as good HIs for capacity estimation.

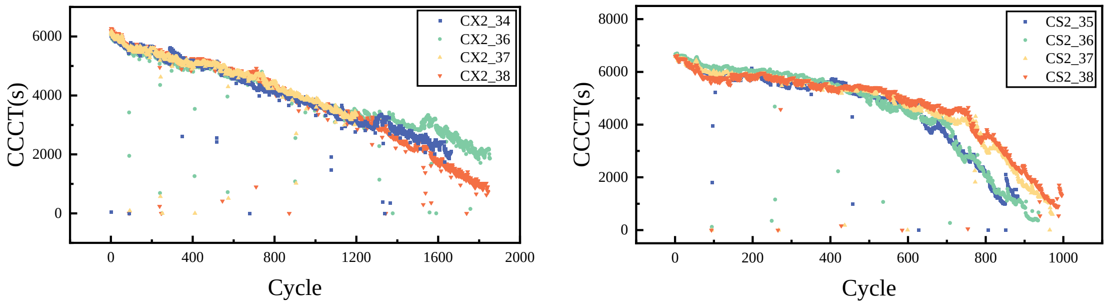

(a) (b)

Figure 11. (a) CX2 batteries (b) CS2 batteries constant current charging time

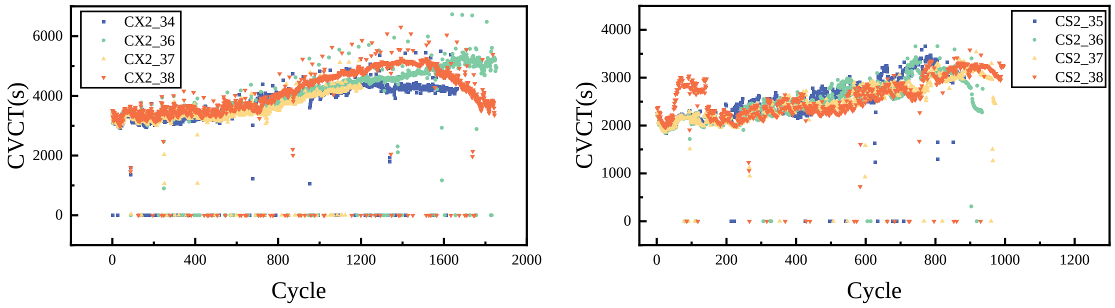

(a) (b)

Figure 12. (a) CX2 batteries (b) CS2 batteries constant voltage charging time

From Figure 13 and Figure 14, it can be seen that as the battery aging experiment proceeds, the available capacity of the battery gradually decreases, while the resistance of the internal resistance of the battery also gradually increases. The phenomenon that the electrode potential deviates from the equilibrium electrode potential when current is passed through the electrode is called electrode polarization. Polarization includes ohmic polarization, electrochemical polarization, and concentration polarization. The polarization resistance is the internal resistance caused by the polarization of the positive and negative electrodes of the battery during the electrochemical reaction, which can reflect the internal consistency of the battery, but it is not applicable in production due to the influence of operation and method. The internal resistance of polarization is not constant and changes over time during the charging and discharging process because the composition of the active material, the concentration of the electrolyte, and the temperature are constantly changing. The ohmic internal resistance obeys Ohm's law, and the polarized internal resistance increases with the increase of current density, but it is not a linear relationship. It often increases linearly with the logarithm of the current density.

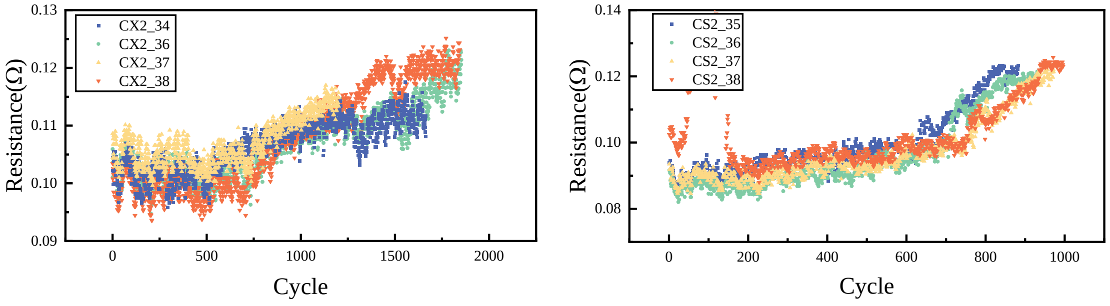

(a) (b)

Figure 13. (a) CX2 (b) CS2 battery pack internal resistance change graph

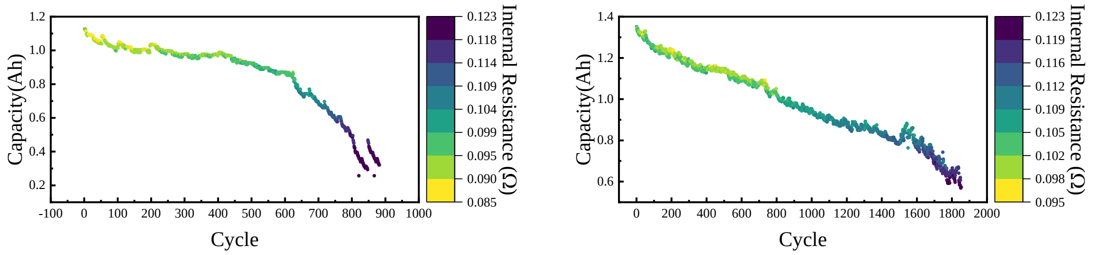

(a) (b)

Figure 14. (a) CS2_35 (b) CX2_36 battery aging process resistance change graph

The concept of incremental capacity (IC) analysis was first introduced by Thompson and applied to materials research [30], and in recent years it has only been used for battery SOH estimation. In the study of lithium battery capacity degradation, the IC curve represents the increment of battery power per unit voltage. Theoretically, it is derived from the U-Q curve, but in practical applications, the derivation of discrete data is usually calculated by the difference method with the equation shown in Equation (26).

$$IC = \frac{dQ}{dU} \approx \frac{\Delta Q}{\Delta U} \tag{26}$$

Where Q is the battery capacitance, U is the battery voltage, I is the battery current.

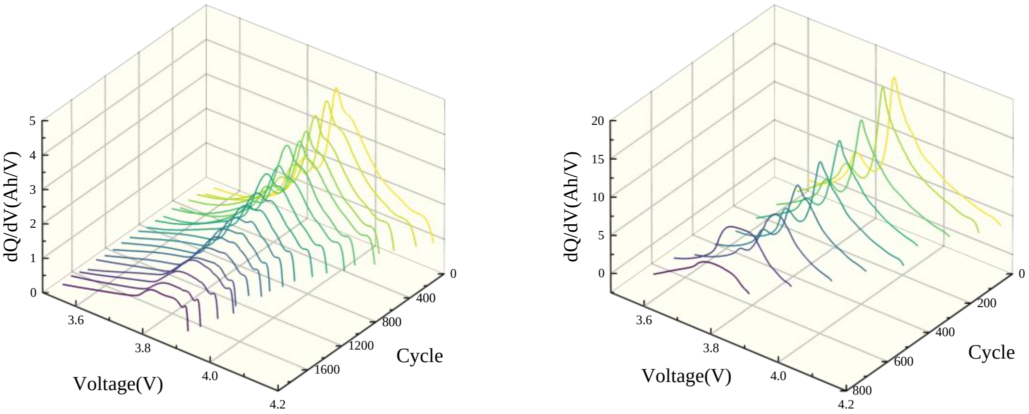

(a) (b)

Figure 15. (a) CX2_36 (b) CS2_35 Partial IC curve extraction diagram

Analysis of the reasons for the increase of the internal resistance of the battery, the loss of electrolyte, the blockage of the diaphragm micropores, the continuous thickening of the SEI film and CEI film, the precipitation of lithium dendrites on the surface of the negative electrode, the structural damage caused by the leaching of metals from the positive electrode material, the poor contact between the part of the active material and the collector, etc. due to the volume change of the graphite negative electrode, the flaking of graphite particles due to the co-embedding of the electrolyte and lithium ions, and the corrosion of the collector and the adhesive are all possible reasons for the increase of the internal resistance. With the cyclic aging process, the loss of lithium ions and active materials occurs inside the battery, the ohmic voltage drop, and the polarization voltage inside the battery increase, and the result is an increase in the voltage plateau during battery charging. As the lithium battery charging voltage curve is flat, the difference cannot be directly observed, and after transforming into the capacity increment curve, it can be found that the overall shift of the capacity increment curve to the left occurs, indicating the decrease of the voltage plateau during battery charging.

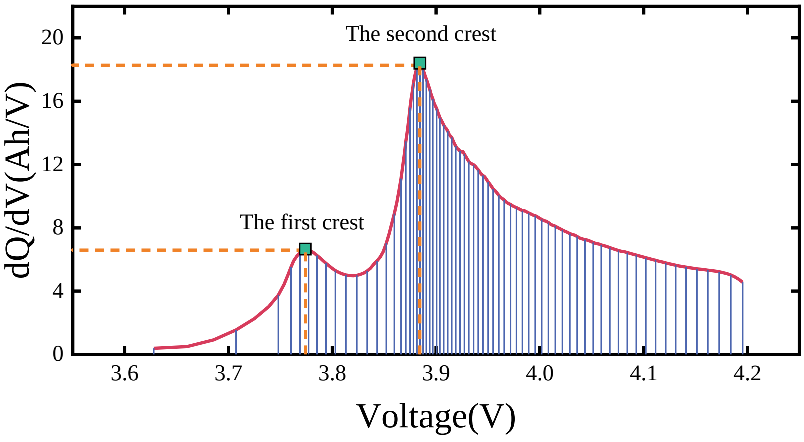

Figure 16. CS2_35 battery IC curve at 50 cycles

As shown in Figure 16, the IC curve of the CS2_35 battery pack at the 50th cycle shows two obvious peaks, while as shown in Figure 15, with the aging experiments of the Lithium-ion battery, the IC curve shows only one peak. Therefore, to minimize the extraction error, this paper chooses to extract the IC value with the largest peak as the health indicator ICCP.

From Figure 17, it can be seen that the extracted ICCP shows a significant downward trend, which is consistent with the previous analysis because when the battery aging phenomenon occurs, it leads to a decrease in the voltage plateau of the battery charging process. The Pearson correlation analysis can be concluded that it has a strong correlation with the battery capacity.

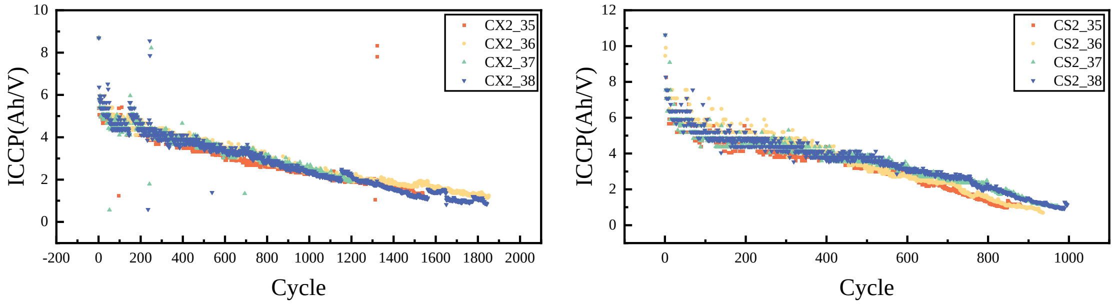

(a) (b)

Figure 17. (a) CX2 (b) CS2 extracting peak dQ/dV values from IC curve

By conducting Pearson correlation analysis on the extracted features of the ten battery groups, as shown in Equation (27), when the absolute value of the correlation coefficient is greater than 0.8, the two variables are strongly correlated, indicating that the extracted HIs all have high correlation and are suitable for the estimation of battery health status, and the correlation results are shown in Figure 18 below.

$$P=\frac{\sum_{i=1}^{n}(X_A^i-\overline{X}_A)(X_B^i-\overline{X}_B)}{\sqrt{\sum_{i=1}^{n}(X_A^i-\overline{X}_A)^2}\sqrt{\sum_{i=1}^{n}(X_B^i-\overline{X}_B)^2}} \tag{27}$$

where X_A^i is the *i*-th sample of sample *A* and $\overline{X}_A$ is the mean of sample *A*, X_B^i is the *i*-th sample of sample *B* and $\overline{X}_B$ is the mean of sample *B*, and *P* is the Pearson correlation coefficient.

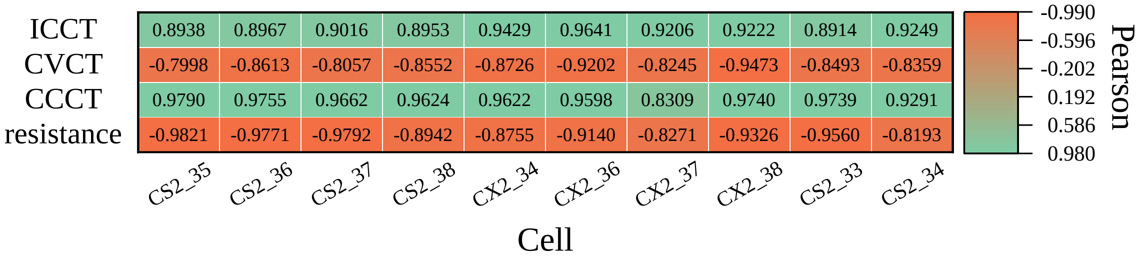

	CS2_35	CS2_36	CS2_37	CS2_38	CX2_34	CX2_36	CX2_37	CX2_38	CS2_33	CS2_34
ICCT	0.8938	0.8967	0.9016	0.8953	0.9429	0.9641	0.9206	0.9222	0.8914	0.9249
CVCT	-0.7998	-0.8613	-0.8057	-0.8552	-0.8726	-0.9202	-0.8245	-0.9473	-0.8493	-0.8359
CCCT	0.9790	0.9755	0.9662	0.9624	0.9622	0.9598	0.8309	0.9740	0.9739	0.9291
resistance	-0.9821	-0.9771	-0.9792	-0.8942	-0.8755	-0.9140	-0.8271	-0.9326	-0.9560	-0.8193

Figure 18. Pearson correlation coefficient plot of relevant health indicators against battery capacity

4. Experimental results

The SOH level is described by the capacity degradation characteristic, from which the end-of-life (EOL) value is calculated and taken to be 80% of the rated capacity. Specific information on the relationship between SOH and RUL is shown in Figure 19.

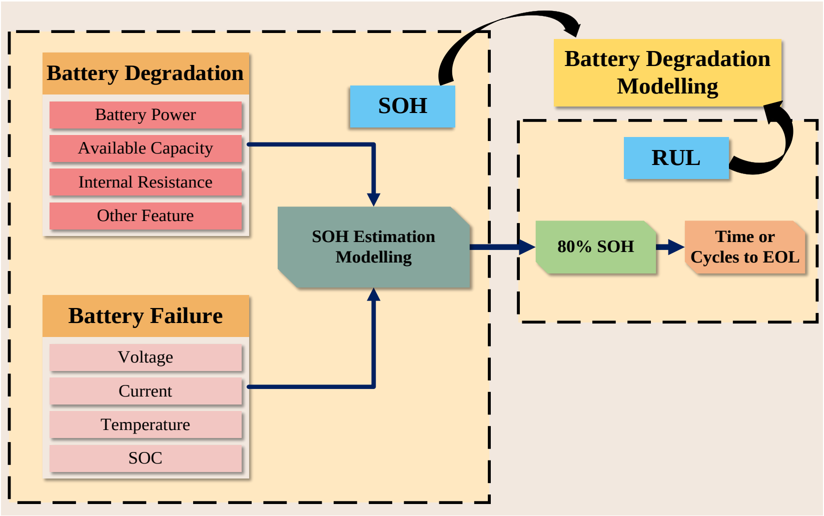

Figure 19. SOH and RUL relationship diagram

$$y_{SOH} = \frac{C_n}{C_{initial}} \times 100\% \tag{28}$$

$$EOL = C_{initial} \times 0.8 \tag{29}$$

$$\begin{cases} RUL_T = n_{EOL}^T - n_t \\ RUL_P = n_{EOL}^P - n_t \end{cases} \tag{30}$$

$$E_{RUL} = RUL_T - RUL_P \tag{31}$$

y_{SOH} is the real SOH, C_n is the current capacity and $C_{initial}$ is the initial capacity of the battery. RUL_T is the RUL value measured from the experimental data and RUL_P is the RUL value predicted from the data-driven model. n_{EOL}^T is the number of EOL cycles measured experimentally. n_{EOL}^P is the number of *EOL* cycles predicted by the prediction program. n_t is the current number of cycles. E_{RUL} is the prediction error or residual.

In this experiment, root mean square error (*RMSE*) and coefficient of determination (R^2) values were used to verify the accuracy of the prediction and the model. The error (E_{RUL}), mean absolute error (*MAE*), and mean absolute percentage error (*MAPE*) was also introduced for performance evaluation. The calculation process of the error evaluation index is mathematically expressed in the following equation:

$$MAE = \frac{1}{N}\sum_{k=1}^{N} \left| \hat{y}_{SOH} - y_{SOH} \right| \tag{32}$$

$$RMSE = \sqrt{\frac{1}{N}\sum_{k=1}^{N} \left(\hat{y}_{SOH} - y_{SOH} \right)^2} \tag{33}$$

$$MAPE = \frac{100\%}{N}\sum_{k=1}^{N}\left|\frac{\hat{y}_{SOH} - y_{SOH}}{y_{SOH}}\right| \qquad (34)$$

where $\hat{y}_{SOH}$ is the SOH value predicted by the data-driven model.

Figure 20 shows the SOH prediction results of the experimental data of the CS2 battery pack of 35, 36, 37, and 38 cells under the condition of constant current discharge aging at 1℃, i.e., the prediction results of the four algorithms in sequence, and it can be seen that the experimental curve of the IGWO-DELM algorithm follows the best, and the error is also shown to be the smallest and closest to 0, which indicates the optimization effect of SCA on the GWO algorithm. It can well prevent GWO from falling into the local optimum in the process of finding the optimum so that the global optimum can be found to obtain better training results. The details of Figure 20 also show that the errors of improved GWO-DELM remain very good from the beginning to the end, all converging to Figure 21 shows the RMSE, MAE, and MAPE values of the four cells, and it can be seen that the accuracy of the algorithm is improved with the optimization of the superposition, and the prediction effect of the GWO algorithm is enhanced with the addition of the SCA algorithm. The experimental results of the four cells show that the IGWO-DELM predicts SOH and RUL superiorly, and the analysis of the results shows that MAE is below 2%, RMSE is below 2.5%, and MAPE is below 2.5%, all of which are kept at a low level. Table 2 shows, the results of RUL prediction for the CS2 battery pack, indicating that the prediction error EOL cycle number of IGWO-DELM is the closest among the four algorithm estimates and the most accurate prediction, showing the robustness and accuracy of IGWO-DELM algorithm.

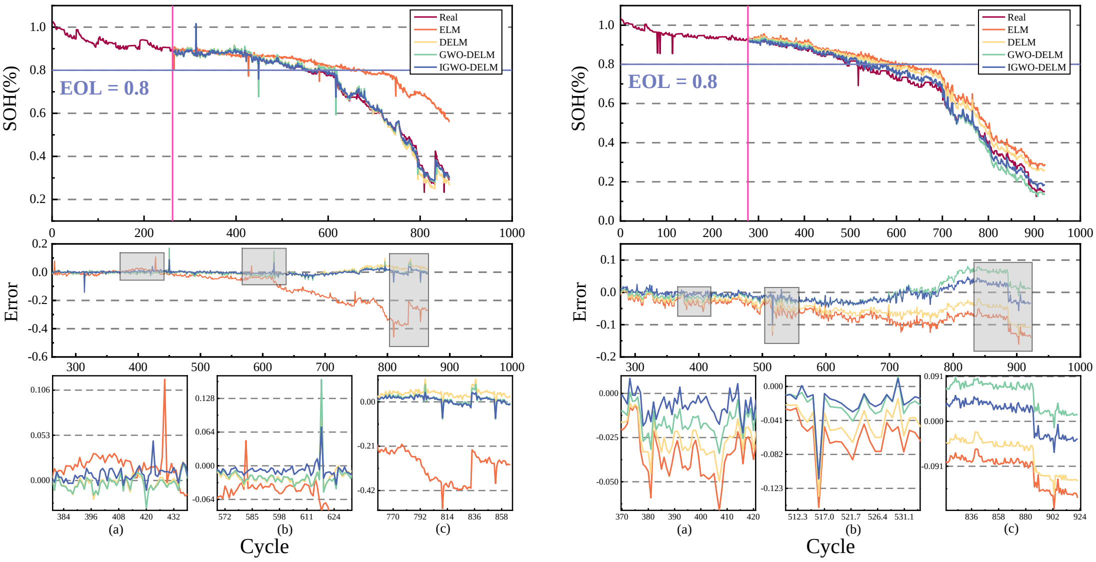

(a) (b)

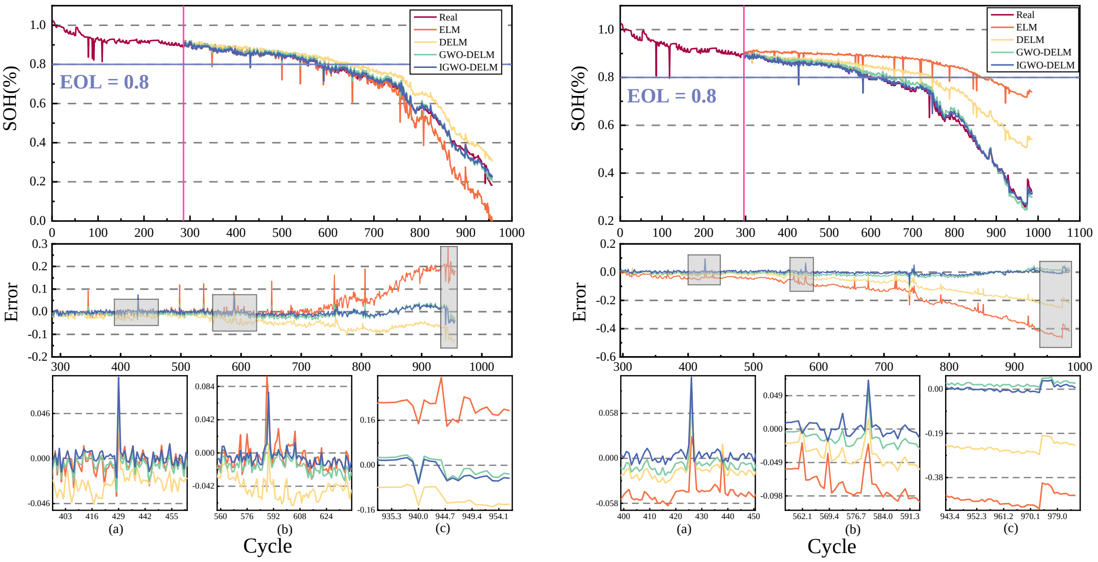

(c)

(d)

Figure 20. (a) CS2_35 battery (b) CS2_36 battery (c) CS2_37 battery (d) CS2_38 battery comparison experimental results and error details graph

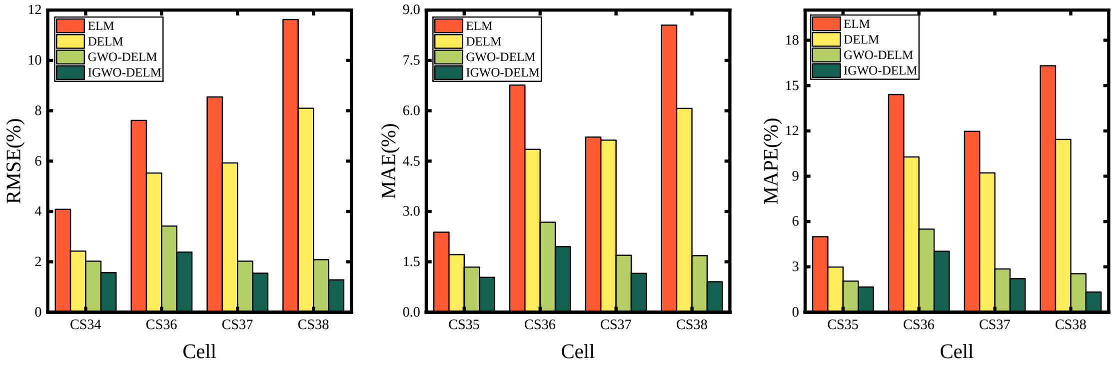

(a)

(b)

(c)

Figure 21. (a) RMSE (b) MAE (c) MAPE analysis of RUL forecast results

Table 2. RUL prediction results for CS2 battery pack cycled at a constant current of 1℃

Battery name	Model	EOL Cycle	Absolute Error	Estimate Cycle	RMSE	MAE	MAPE
CS2_35	ELM	515	21	537	0.041	0.024	0.050
	DELM		76	591	0.024	0.017	0.030
	GWO-DELM		65	580	0.020	0.013	0.021
	IGWO-DELM		28	543	0.016	0.010	0.017
CS2_36	ELM	484	83	567	0.076	0.068	0.144
	DELM		65	549	0.055	0.049	0.103
	GWO-DELM		29	513	0.034	0.027	0.055
	IGWO-DELM		29	513	0.024	0.020	0.040
CS2_37	ELM	565	18	583	0.086	0.052	0.120
	DELM		52	617	0.059	0.051	0.092
	GWO-DELM		18	583	0.020	0.017	0.029
	IGWO-DELM		11	576	0.015	0.012	0.022
CS2_38	ELM	574	138	712	0.116	0.086	0.163
	DELM		24	598	0.081	0.061	0.114

GWO-DELM	54	628	0.021	0.017	0.025
IGWO-DELM	1	573	0.013	0.009	0.013

Figure 22 shows the SOH prediction results obtained from the SOH prediction results obtained by the data-driven model output with the input of extracted HIs for the four cells of CX2 batteries 34, 36, 37, and 38 discharged at constant current at 0.5℃. It can be seen that the IGWO-DELM algorithm shows a clear advantage among the four compared algorithms, maintaining high robustness and high accuracy. The error detail plot shows that IGWO-DELM has maintained low error in the test set, and it can be seen in Figure 23 that the SOH prediction results of IGWO-DELM are also at a better level for all indicators, with MAE below 3%, RMSE below 3.5%, and MAPE below 4% in all four batteries. The data of the four batteries in Table 3 also show that the RUL prediction ability of IGWO-DELM is ranked first among the four algorithms.

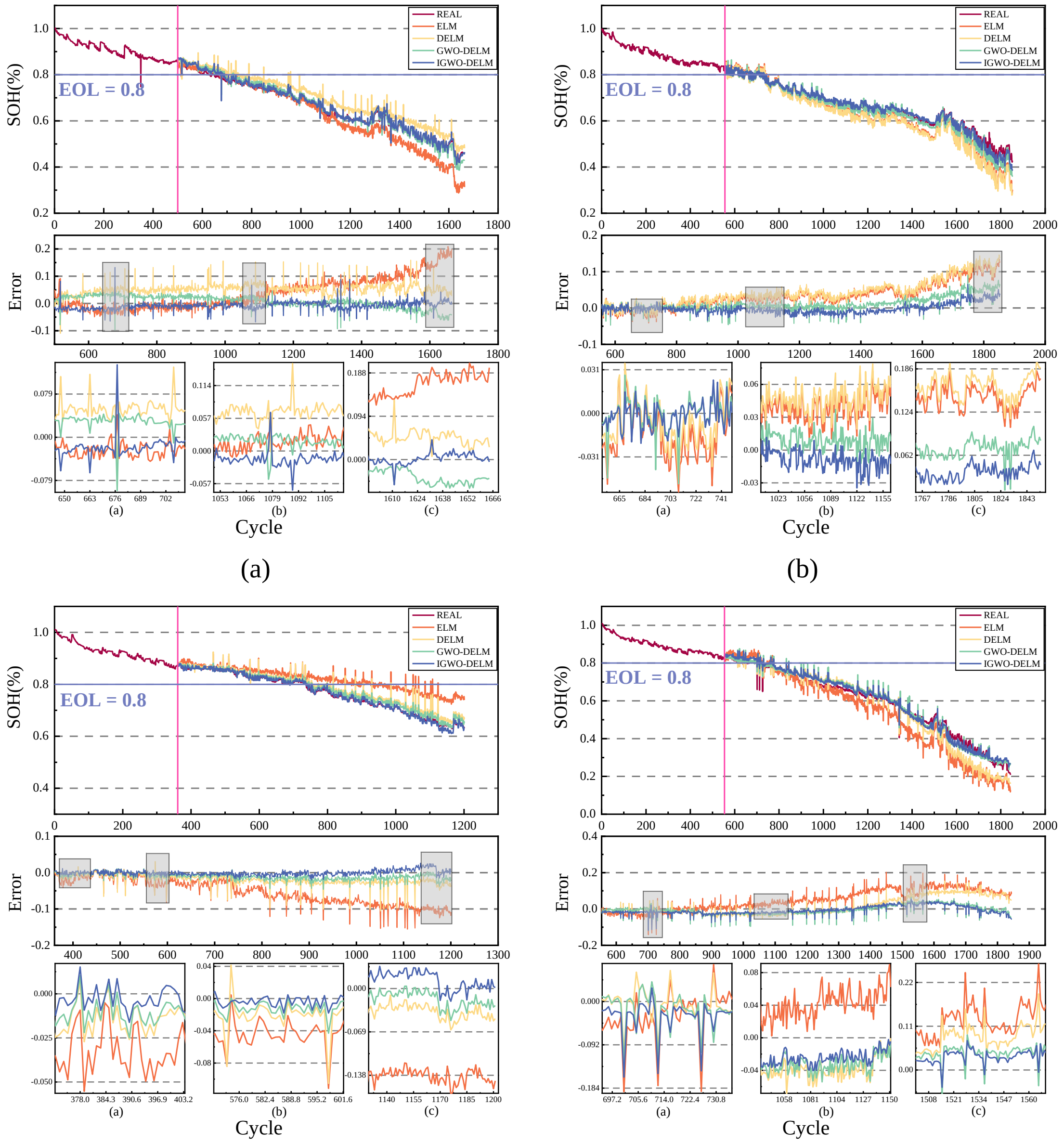

(a) (b)

(c) (d)

Figure 22. (a) CX2_34 battery (b) CX2_36 battery (c) CX2_37 battery (d) CX2_38 battery comparison experimental results and error details graph

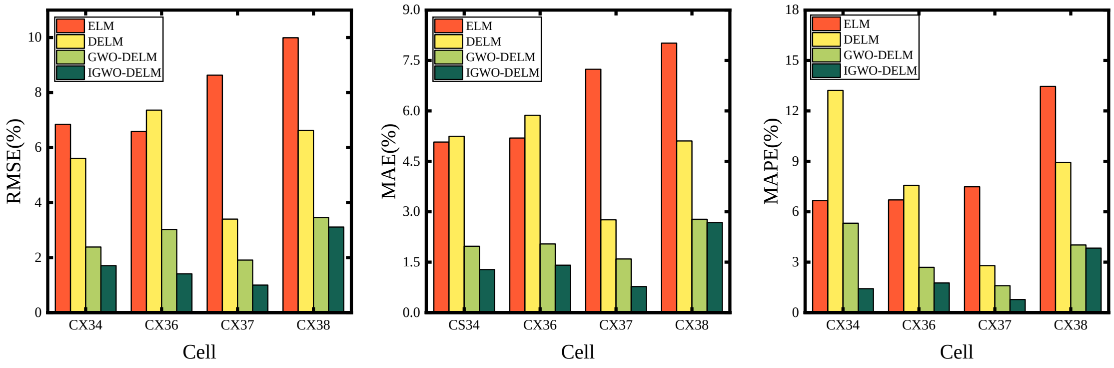

(a) (b) (c)

Figure 23. (a) RMSE (b) MAE (c) MAPE analysis of RUL forecast results

Table 3. RUL prediction results for CX2 battery pack cycled at a constant current of 0.5℃

Battery name	Model	EOL Cycle	Absolute Error	Estimate Cycle	RMSE	MAE	MAPE
CX2_34	ELM	648	83	731	0.068	0.051	0.067
	DELM		312	960	0.056	0.052	0.132
	GWO-DELM		78	726	0.024	0.020	0.053
	IGWO-DELM		40	688	0.017	0.013	0.014
CX2_36	ELM	734	10	744	0.066	0.052	0.067
	DELM		11	745	0.074	0.059	0.076
	GWO-DELM		0	734	0.030	0.020	0.027
	IGWO-DELM		3	737	0.014	0.014	0.018
CX2_37	ELM	736	372	1108	0.086	0.072	0.075
	DELM		194	930	0.034	0.028	0.028
	GWO-DELM		153	583	0.019	0.016	0.016
	IGWO-DELM		0	736	0.010	0.008	0.008
CX2_38	ELM	711	59	770	0.100	0.080	0.135
	DELM		1	710	0.066	0.051	0.089
	GWO-DELM		133	844	0.035	0.028	0.040
	IGWO-DELM		65	776	0.031	0.027	0.038

Figure 24 shows the experimental SOH results for cells 33 and 34 in the CS2 battery pack with constant current discharge at 0.5℃. The SCA optimization of GWO significantly improves the global optimal solution of DELM, and it can be seen that the SOH prediction curves of IGWO-DELM follow the experimentally obtained cell capacity curves very closely, which reflects the excellent performance of IGWO. The comparison in Figure 25 shows that the MAE, RMSE, and MAPE values of IGWO are better than those of the other three comparative algorithms. The RUL prediction EOL error shown in Table 4 is also the lowest among the four algorithms.

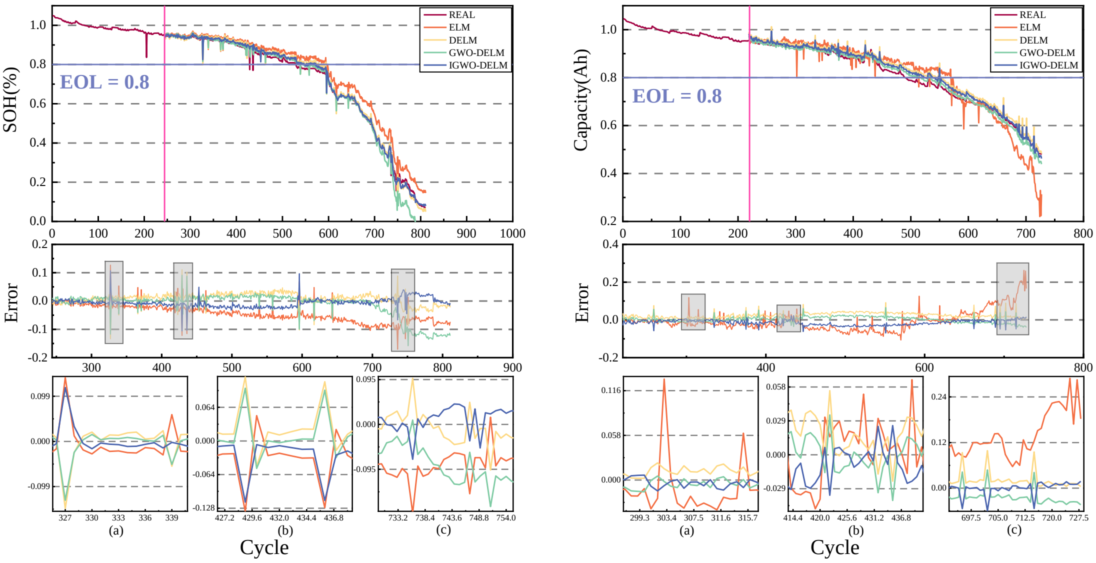

(a) (b)

Figure 24. (a) CS2_33 battery (b) CS2_34 battery comparison experimental results and error details graph

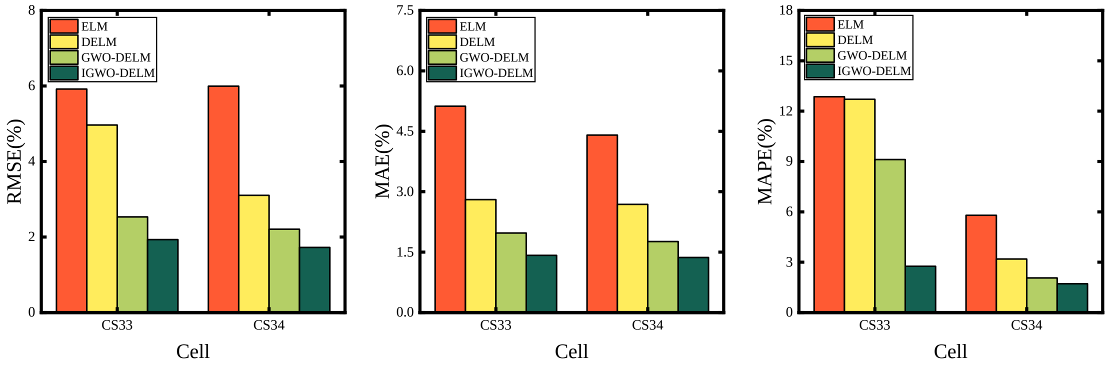

(a) (b) (c)

Figure 25. (a) RMSE (b) MAE (c) MAPE analysis of RUL forecast results

Table 4. RUL prediction results for CS2 battery pack cycled at a constant current of 0.5℃

Battery name	Model	EOL cycle	Absolute Error	Estimate Cycle	RMSE	MAE	MAPE
CS2_33	ELM	501	71	572	0.059	0.051	0.129
	DELM		28	529	0.050	0.028	0.127
	GWO-DELM		4	505	0.025	0.020	0.091
	IGWO-DELM		5	506	0.019	0.014	0.028
CS2_34	ELM	448	99	547	0.060	0.044	0.058
	DELM		102	550	0.031	0.027	0.032
	GWO-DELM		102	550	0.022	0.018	0.021
	IGWO-DELM		37	572	0.017	0.014	0.017

5. Conclusion

In this paper, a data-driven model based on deep extreme learning machine and improved Gray Wolf optimization algorithm is proposed to process the capacity data of lithium-ion batteries and predict the health state and remaining service life of the batteries. The model aims to predict the SOH and RUL of lithium-ion batteries using experimentally measured battery capacity and HIs extracted from the analysis of experimental data. The CALCE Data Center of the University of Maryland's open data set, which contains 10 experimental data sets of CS2 and CX2 batteries, is used in this study.

At the same time, this paper proposed a multi-scale feature extraction method to extract the characteristics of battery constant-current charging time, constant-voltage charging time, and internal resistance from the current-voltage experimental data, and analyzed the IC curve of charge and discharge stage to extract the relevant features, and verified the strength of the correlation using Pearson correlation coefficient equation. In the previous mechanism analysis and curve comparison, it was found that the curve of some data has an obvious downward trend or fluctuation trend with the aging degree of the battery, that is, the extracted features can reflect the degradation process of the lithium-ion battery. These characteristics are based on the battery aging experiment charge and discharge test data and the attenuation mechanism of the electrochemical battery, and achieve high precision optimized data-driven.

The extracted battery capacity and lithium-ion battery HIs were input into the IGWO-DELM data-driven model for SOH prediction. It can be seen from the experimental output that with the enhancement of the optimization model, the evaluation indexes of the optimization and improvement model are significantly reduced, and the RMSE of the test battery is lower than 4%, MAPE is lower than 3.8%, and MAE is lower than 2.7%, which verifies the effectiveness and robustness of the algorithm. And can accurately predict the decline of battery health. In future work, further study of SOH estimation using partially charged or discharged battery data will be a feature work. This work can provide a solution to the practical application problem of LIBs in the case of partial charge or discharge.

References

1. Ge, M.-F., et al., *A review on state of health estimations and remaining useful life prognostics of lithium-ion batteries.* Measurement, 2021. **174**: p. 109057.
2. Wang, Y.J., X.C. Zhang, and Z.H. Chen, *Low temperature preheating techniques for Lithium-ion batteries: Recent advances and future challenges.* Applied Energy, 2022. **313**.
3. Hu, X., et al., *State estimation for advanced battery management: Key challenges and future trends.* Renewable and Sustainable Energy Reviews, 2019. **114**: p. 109334.
4. Zhou, C.-C., et al., *Ultra-high-energy lithium-ion batteries enabled by aligned structured thick electrode design.* Rare Metals, 2022. **41**(1): p. 14-20.
5. Chang, C., et al., *Prognostics of the state of health for lithium-ion battery packs in energy storage applications.* Energy, 2022. **239**: p. 122189.
6. Wang, Y., et al., *Perspectives and challenges for future lithium-ion battery control and management*. 2023, Elsevier.
7. Cheng, G., X. Wang, and Y. He, *Remaining useful life and state of health prediction for lithium batteries based on empirical mode decomposition and a long and short memory neural network.* Energy, 2021. **232**: p. 121022.
8. Li, X., et al., *Remaining useful life prediction for lithium-ion batteries based on a hybrid model combining the long short-term memory and Elman neural networks.* Journal of Energy Storage, 2019. **21**: p. 510-518.
9. Zhang, Y., et al., *Validation and verification of a hybrid method for remaining useful life*

prediction of lithium-ion batteries. Journal of Cleaner Production, 2019. **212**: p. 240-249.

10. Wang, Y., et al., *Health Diagnosis for Lithium-Ion Battery by Combining Partial Incremental Capacity and Deep Belief Network during Insufficient Discharge Profile.* IEEE Transactions on Industrial Electronics, 2022.
11. Schmitt, J., et al., *Impedance change and capacity fade of lithium nickel manganese cobalt oxide-based batteries during calendar aging.* Journal of Power Sources, 2017. **353**: p. 183-194.
12. Xiong, R., et al., *Lithium-ion battery aging mechanisms and diagnosis method for automotive applications: Recent advances and perspectives.* Renewable and Sustainable Energy Reviews, 2020. **131**: p. 110048.
13. Li, J., et al., *A single particle model with chemical/mechanical degradation physics for lithium ion battery State of Health (SOH) estimation.* Applied energy, 2018. **212**: p. 1178-1190.
14. Ye, L., et al., *Effective regeneration of high-performance anode material recycled from the whole electrodes in spent lithium-ion batteries via a simplified approach.* Green Energy & Environment, 2021. **6**(5): p. 725-733.
15. Li, L., et al., *Lithium-ion battery cathode and anode potential observer based on reduced-order electrochemical single particle model.* Journal of Energy Storage, 2021. **44**: p. 103324.
16. Tian, J., Y. Wang, and Z. Chen, *An improved single particle model for lithium-ion batteries based on main stress factor compensation.* Journal of Cleaner Production,

2021. **278**: p. 123456.

17. Rauf, H., M. Khalid, and N. Arshad, *Machine learning in state of health and remaining useful life estimation: Theoretical and technological development in battery degradation modelling.* Renewable and Sustainable Energy Reviews, 2022. **156**: p. 111903.
18. Khaleghi, S., et al., *Developing an online data-driven approach for prognostics and health management of lithium-ion batteries.* Applied Energy, 2022. **308**: p. 118348.
19. Liu, Y., et al., *A novel remaining useful life prediction method for lithium-ion battery based on long short-term memory network optimized by improved sparrow search algorithm.* Journal of Energy Storage, 2023. **61**: p. 106645.
20. Pang, X., et al., *A novel hybrid model for lithium-ion batteries lifespan prediction with high accuracy and interpretability.* Journal of Energy Storage, 2023. **61**: p. 106728.
21. Dang, W., et al., *An encoder-decoder fusion battery life prediction method based on Gaussian process regression and improvement.* Journal of Energy Storage, 2023. **59**: p. 106469.
22. Chen, L., et al., *Remaining useful life prediction of lithium-ion battery using a novel particle filter framework with grey neural network.* Energy, 2022. **244**: p. 122581.
23. Goh, H.H., et al., *Estimation of the state of health (SOH) of batteries using discrete curvature feature extraction.* Journal of Energy Storage, 2022. **50**: p. 104646.
24. Dong, G., W. Han, and Y. Wang, *Dynamic Bayesian network-based lithium-ion battery health prognosis for electric vehicles.* IEEE Transactions on Industrial Electronics, 2020. **68**(11): p. 10949-10958.

25. Kong, J.-z., et al., *Voltage-temperature health feature extraction to improve prognostics and health management of lithium-ion batteries.* Energy, 2021. **223**: p. 120114.

26. Li, H., et al., *Remaining useful life prediction using multi-scale deep convolutional neural network.* Applied Soft Computing, 2020. **89**: p. 106113.

27. Huang, G.-B., Q.-Y. Zhu, and C.-K. Siew, *Extreme learning machine: theory and applications.* Neurocomputing, 2006. **70**(1-3): p. 489-501.

28. Li, Q., et al., *A multi-step ahead photovoltaic power prediction model based on similar day, enhanced colliding bodies optimization, variational mode decomposition, and deep extreme learning machine.* Energy, 2021. **224**: p. 120094.

29. Elghandour, A.N., et al., *An image encryption algorithm based on bisection method and one-dimensional piecewise chaotic map.* IEEE Access, 2021. **9**: p. 43411-43421.

30. Xie, Q., et al., *Optimization of heliostat field distribution based on improved Gray Wolf optimization algorithm.* Renewable Energy, 2021. **176**: p. 447-458.

31. Abualigah, L. and A. Diabat, *Advances in sine cosine algorithm: a comprehensive survey.* Artificial Intelligence Review, 2021. **54**(4): p. 2567-2608.

32. He, W., et al., *Prognostics of lithium-ion batteries based on Dempster–Shafer theory and the Bayesian Monte Carlo method.* Journal of Power Sources, 2011. **196**(23): p. 10314-10321.

33. Li, X., et al., *State-of-health estimation for Li-ion batteries by combing the incremental capacity analysis method with grey relational analysis.* Journal of Power Sources, 2019. **410**: p. 106-114.